



ASME Accepted Manuscript Repository

Institutional Repository Cover Sheet

Theodossiades, Stephanos

First

Last

ASME Paper Title: A nonlinear concept of electromagnetic energy harvester for rotational applications

Authors: [Ben Gunn](#), [Stephanos Theodossiades](#) and [Steve J Rothberg](#)

ASME Journal Title: Journal of Vibration and Acoustics

Volume/Issue 141(3), 031005 Date of Publication (VOR* Online) February 4, 2019

ASME Digital Collection URL: <http://vibrationacoustics.asmedigitalcollection.asme.org/article.aspx?articleid=271653>

DOI: 10.1115/1.4042040

*VOR (version of record)

A Nonlinear Concept of Electromagnetic Energy Harvester for Rotational Applications

B. E. Gunn

Wolfson School of Mechanical, Electrical and Manufacturing Engineering

Loughborough University

Loughborough

LE11 3TU

United Kingdom

B.E.Gunn@lboro.ac.uk

S. Theodossiades¹

Wolfson School of Mechanical, Electrical and Manufacturing Engineering

Loughborough University

Loughborough

LE11 3TU

United Kingdom

S.Theodossiades@lboro.ac.uk

S. J. Rothberg

Wolfson School of Mechanical, Electrical and Manufacturing Engineering

Loughborough University

Loughborough

LE11 3TU

United Kingdom

S.J.Rothberg@lboro.ac.uk

¹ Corresponding author

Abstract

Many industrial applications incorporate rotating shafts with fluctuating speeds around a required mean value. This often harmonic component of the shaft speed is generally detrimental, since it can excite components of the system, leading to large oscillations (and potentially durability issues), as well as to excessive noise generation. On the other hand, the addition of sensors on rotating shafts for system monitoring or control poses challenges due to the need to constantly supply power to the sensor and extract data from the system. In order to tackle the requirement of powering sensors for structure health monitoring or control applications, this work proposes a nonlinear vibration energy harvester design intended for use on rotating shafts with harmonic speed fluctuations. The essential nonlinearity of the harvester allows for increased operating bandwidth, potentially across the whole range of the shaft's operating conditions.

INTRODUCTION

Many industrial applications with rotating shafts exhibit fluctuations around the desired shaft speed, which are generally undesirable and represent energy excess. The latter may be sufficient to excite other propulsion subsystems (leading to excessive vibrations and durability issues) and require palliative measures in the form of vibration dampers resulting in a loss of energy from the system. Meanwhile, wireless sensor nodes are becoming increasingly omnipresent due to new technologies reducing cost and power consumption. In several engineering applications involving rotating shafts, there is a demand for wireless sensors, such as a strain gauge or accelerometer for structural health monitoring systems that are mounted on the rotating

shaft. Currently, batteries or brushed electrical contacts can be employed to power such sensors on rotating shafts. However, these need regular maintenance and replacement, which can be costly and inconvenient. Energy harvesting can recover part of the waste vibration energy and use it to power wireless sensors, thus eliminating the need for batteries or brushed electrical contacts.

Typically, a vibration energy harvester is designed to operate at its resonant frequency which is tuned to match the dominant frequency of the host structure. However, should the vibrations of the host structure deviate from the resonant frequency of the harvester, the amount of harvested energy will be insufficient to power the sensor. For this reason, research efforts have been dedicated in developing energy harvesters that operate over wider frequency ranges (e.g. by introducing nonlinearities).

Several studies in the literature have dealt with energy harvesting from rotating shafts. Commonly, a piezoelectric cantilever beam with a tip mass is mounted on the shaft pointing radially outwards. The cantilever is excited by gravity as the shaft rotates [1–3]. In this configuration, as the shaft speed increases, the centripetal acceleration of the tip mass also increases, effectively increasing the stiffness and therefore the resonant frequency of the system. Through careful selection of the length of the beam and its radial position, the increase in resonant frequency can match the excitation frequency such that resonance occurs through a broad range of shaft speeds. Variations to this configuration have been explored. Zhang et al [4,5] introduced a magnetic tip mass with a repelling magnet mounted to the frame which rotated with the shaft. A bi-stable system resulted which increased the operating frequency range even further than a self-tuning cantilever beam alone.

Gu and Livermore [6] developed a (relatively) stiff piezoelectric beam alongside another (relatively) flexible beam. As the latter deforms, its tip mass impacts the piezoelectric beam. The flexibility of the striking beam

allowed for the resonant frequency to match the driving frequency at all examined speeds, which was proven experimentally up to 17 Hz. Similarly, Roundy and Tola [7] used a ball in a curved track to act as an offset pendulum. At the centre of the track there are piezoelectric beam elements which are plucked as the ball passes over them. The resonant frequency of the pendulum can be tuned to substantially broaden the operating speed range such that it can power a sensor to transmit data for a tyre pressure monitoring system at least once per minute from 10-155 km/h. Wang et al [8] used a weighted pendulum energy harvester with an axial flux permanent magnet generator for a tyre pressure monitoring system which generated 200-300 μW between 200-400 rpm wheel speed.

Rotational energy harvesting technologies are also employed in wind energy applications, where shaft speeds are generally low and variable. Yang et al [8] used steel balls to impact piezoelectric cantilevers arranged in a circle. Zhang et al [9] also used piezoelectric impacts as a frequency up-conversion by mounting a triangular spatula in the centre of piezoelectric cantilevers that are struck as the triangular turntable rotates. Joyce et al [10] used a magnet falling through a coil to generate up to 3.3 mW at 44 rpm from the mean shaft speed of a wind turbine blade. Beyond a certain speed of the wind turbine, the centripetal acceleration exceeds the gravitational acceleration and the magnet is unable to fall through the coil.

All the energy harvesters discussed so far have extracted their energy from the mean shaft speed rather than the shaft speed fluctuations. To harness energy in a watch from the swinging motion of an arm, Pillatsch et al [11,12] developed a frequency up converting piezoelectric cantilever which was plucked by contactless interactions between a magnetic pendulum and a magnetic proof mass. They observed poor longevity of the device due to overstressing the piezoelectric beam, but they did generate up to 43 μW at 2 Hz when the acceleration of the shaft was 20 m/s^2 and the pendulum swung through a full rotation. Mei and Li [13] created a T-shaped piezoelectric energy harvester which was excited by a torsional base oscillation. Piezoelectric

elements were bonded to a steel substrate with steel proof masses such that the torsional oscillations cause a twisting of the piezoelectric beam area. Such a device exhibits a linear resonant frequency response and was reported to generate 23 mW at a resonant frequency of about 252 Hz .

Trimble et al [14] used a linear spring attached to an electromagnetic generator to harness random vibrations encountered in oil rig drilling. Their harvester can generate 205 mW at resonance and 74 mW for random excitations that would be experienced when drilling. Kim [15] used the piezoelectric cantilever design except it was tuned to harvest the torsional speed fluctuations of an internal combustion engine rather than its mean shaft speed. This speed fluctuation is caused by discontinuous combustion and the geometry of a crank shaft and is dependent on the shaft speed which should allow for appropriate tuning. This experimental prototype generated 14 μ W at resonance which was deemed insufficient to power a wireless strain gauge torque sensor.

The authors are not aware of any previously published work describing an electromagnetic energy harvester that employs nonlinearities to maximise its operational frequency range for use in a propulsion shaft that exhibits torsional speed fluctuations. This work presents a novel energy harvester, based on the duffing-oscillator, which uses a brushless permanent magnet motor as an electromechanical coupling element. The exploitation of the nonlinear (duffing) oscillator allows for a broader operating frequency range compared to previously published literature on rotational electromagnetic electromechanical coupling devices. First, the operating principles of the harvester are outlined and the governing equations are developed. A parametric study of the main variables of the harvester is followed by an optimisation process for intended use in rotating shaft applications with a harmonic speed fluctuation.

The Proposed Energy Harvester

In this section, the equations of motion for the proposed harvester are presented. The resulting equations are similar to that of Trimble et al [14] except with the addition of a cubic stiffness component. In addition, the nonlinear electromagnetic coupling factor has been determined by implementing the work of Markovic et al [16] and was added to the equations of motion using the method derived by Owens and Mann [17].

Fig. 1 shows the proposed arrangement of the energy harvester device. Essentially, the energy harvester is an external rotor brushless permanent magnet dc motor. The motor consists of a stator with series wound coils on each tooth whose absolute angular displacement is denoted as α . A rotor with radially polarised magnets whose polarity alternates between adjacent magnets surrounds the stator and is mounted to the stator by low friction bearings. The absolute displacement of the rotor is denoted β . The relative displacement between the stator and rotor is denoted φ , and is given by

$$\varphi = \alpha - \beta \quad (1)$$

A torsional spring element exhibiting cubic nonlinear stiffness characteristics is mounted between the rotor and the stator. This spring is represented in Fig. 1 by the equivalent spring torque acting on the rotor $k\varphi + k_3\varphi^3$. If the rotor is displaced from its equilibrium position and then released, it will oscillate relative to the stator due to the cubic spring. This relative motion causes a change in the flux through the stator core and hence generates an electromotive force (emf) in the coil. If the stator were to oscillate torsionally, this would excite the rotor to oscillate in relation to it due to the cubic spring. If the stator were to rotate at a constant speed, then the rotor would rotate with it at the same speed (after any transients are eliminated) and there would be no relative motion and hence no generated emf. In the case of the stator rotating at a mean speed with a superimposed harmonic fluctuation, the fluctuations would cause vibrations of the rotor with respect

to the stator and hence generate an emf in the coils. The mean component of the shaft speed will not contribute in the generation of the emf. By attaching the stator to a rotating shaft, torsional oscillations can be converted into useful electrical energy for powering wireless sensor applications.

The shaft to which the energy harvester is attached rotates at a mean speed with a superimposed harmonic fluctuation, as described by equation (2) (which is typical of propulsion systems in many applications):

$$\dot{\alpha} = \Omega + 0.01\Omega\sin(\omega t) \quad (2)$$

where Ω denotes the mean shaft speed in rad/s and ω is the frequency of the harmonic fluctuations. Such speed fluctuations can be observed in drivetrains driven by internal combustion engines, such as in automobiles and ships. The speed fluctuation of 1% is an estimate for ground transportation environment based on available experimental data. For a four-stroke, four-cylinder engine, the dominant frequency of the induced oscillations is known to be twice the shaft mean speed:

$$\omega = 2\Omega \quad (3)$$

Differentiating eqn. (2) with respect to time and substituting eqn. (3) yields:

$$\ddot{\alpha} = 0.005\omega^2\cos(\omega t) \quad (4)$$

The system Lagrangian is used to derive the equations of motion. The kinetic energy, T , is given by:

$$T = \frac{1}{2}J\dot{\beta}^2 + \frac{1}{2}L\dot{q}^2 + T_c \quad (5)$$

where J is the mass moment of inertia of the rotor, L , is the inductance of the coil, $\dot{\beta}$ is the angular velocity of the rotor, \dot{q} is the time rate of change of the electric charge and T_c is the electromagnetic coupling energy

term derived by Owens and Mann [17]. By assuming that eddy current losses, skin effects and capacitance within the coil are negligible, the mechanical coupling energy can be assumed to be equal to the electrical coupling energy, as in [17]. The electrical power is integrated over time to obtain the coupling energy term:

$$T_c = \int_0^t \varepsilon \dot{q} dt = \int_0^t \dot{\varphi} \hat{\theta}(\varphi) \dot{q} dt = \dot{q} \int_0^{\varphi} \hat{\theta}(\varphi) d\varphi \quad (6)$$

where ε denotes the electromotive force (emf) and t denotes time. According to Faraday's law, the emf induced in a closed loop of conductor is equal to the rate of change of the magnetic flux passing through the coil [17]:

$$\varepsilon = \frac{d\Phi_m}{dt} = \frac{d\Phi_m}{d\varphi} \frac{d\varphi}{dt} = \frac{d\Phi_m}{d\varphi} \dot{\varphi} = \hat{\theta}(\varphi) \dot{\varphi} \quad (7)$$

where $\hat{\theta}(\varphi)$ is termed the electromagnetic coupling factor and represents the rate of change of magnetic flux through the coils with respect to the relative displacement of the rotor to the stator. Hereafter $\hat{\theta}(\varphi)$ will be denoted $\hat{\theta}$ for ease of reading; however, it should be made clear that the coupling factor depends on the relative angular displacement of the rotor.

Next, the potential energy function, U , is derived. The capacitance of the coil is negligible, hence the potential energy originates solely from the cubic spring:

$$U = \frac{1}{2} k_1 \varphi^2 + \frac{1}{4} k_3 \varphi^4 \quad (8)$$

where k_1 and k_3 are the linear and nonlinear stiffness coefficients, respectively.

Finally, the energy dissipation terms arise from the electrical resistance and the mechanical damping which includes bearing losses, spring losses and Eddy current losses:

$$D = \frac{1}{2} c_{mech} \dot{\varphi}^2 + \frac{1}{2} (R_{Load} + R_{int}) \dot{q}^2 \quad (9)$$

where c_{mech} denotes the mechanical damping coefficient and R_{Load} and R_{int} are the electrical load and internal resistances, respectively. Using the Lagrange equation:

$$\frac{d}{dt} \left(\frac{\partial T}{\partial \dot{q}_n} \right) - \frac{\partial T}{\partial q_n} + \frac{\partial D}{\partial \dot{q}_n} + \frac{\partial U}{\partial q_n} = Q_n \quad (10)$$

and setting the relative displacement φ as the first generalized coordinate, the following equation of motion is derived:

$$J\ddot{\varphi} = -k_1\varphi - k_3\varphi^3 - c_{mech}\dot{\varphi} + \hat{\theta}I + J\ddot{\alpha} \quad (11)$$

Setting the electric charge q as the second generalized coordinate, the electrical equation is derived:

$$L\dot{I} + (R_{Load} + R_{int})I + \hat{\theta}\dot{\varphi} = 0 \quad (12)$$

where I denotes the current (time rate of change of electric charge, \dot{q}).

Magnetic and Coil Models

When designing magnetic machines, three-dimensional numerical models are ideal to gain an accurate prediction of the motor's performance. However, such models are time- and computing-power intensive;

therefore, for optimisation purposes, two-dimensional analytical models are often used. Certain assumptions need to be valid so that this approach provides reasonable accuracy:

- The axial length of the energy harvester is sufficiently large compared to the air gap so that end effects can be neglected, and the axial component of flux density is negligible.
- All materials are isotropic.
- The permanent magnets exhibit linear second quadrant demagnetization characteristic.
- The iron used in stator core and backing plate is infinitely permeable.

Zhu et al [18] derived an analytical equation for the radial magnetic flux density at the stator iron given the above assumptions:

$B_{rad} =$

$$\sum_{n=1,3,5,\dots}^{\infty} 2 \frac{\mu_0 M_n}{\mu_r} \frac{np}{(np)^2 - 1} \left(\frac{R_s}{R_m}\right)^{np-1} \left[\frac{(np-1)R_m^{2np} + 2R_r^{np+1}R_m^{np-1} - (np+1)R_r^{2np}}{\frac{\mu_r+1}{\mu_r}(R_s^{2np} - R_m^{2np}) - \frac{\mu_r-1}{\mu_r} \left[R_m^{2np} - R_s^{2np} \left(\frac{R_r}{R_m}\right)^{2np} \right]} \right] \sin(np\varphi) \quad (13)$$

In the present work, the assumption is made that when $\varphi = 0$ rad, the centre of the coil is aligned with the gap between one magnet and the next one, such that the net flux through the coil is null. Radial magnetization is assumed based on the geometry of the magnets that will be used. Thus, the magnetization vector M_n is given by eqn. (14) [16]:

$$M_n = 4 \frac{B_r}{\pi \mu_0 n} \sin\left(\frac{n\pi v}{2}\right) \quad (14)$$

Markovic [16] derived the emf of a coil of wire in a radial brushless DC motor using eqn. (13) as:

$$\varepsilon = - \sum_{n=1,3,5,\dots}^{\infty} \frac{1}{k_c} np \phi h N_f K_n T_n \cos(np\phi) \quad (15)$$

where K_n , T_n and k_c are given as follows:

$$K_n = \frac{\mu_0 M_n}{\mu_r} \frac{np}{(np)^2 - 1} \times \frac{(np-1) \left(\frac{R_m}{R_r}\right)^{2np} + 2 \left(\frac{R_m}{R_r}\right)^{np-1} - (np+1)}{\frac{\mu_r + 1}{\mu_r} \left[1 - \left(\frac{R_s}{R_r}\right)^{2np}\right] - \frac{\mu_r - 1}{\mu_r} \left[\left(\frac{R_s}{R_m}\right)^{2np} - \left(\frac{R_m}{R_r}\right)^{2np}\right]} \quad (16)$$

$$T_n = \frac{4}{np} R_s \left(\frac{R_s}{R_m}\right)^{np-1} \sin\left(\frac{np\pi}{N_s}\right) \quad (17)$$

$$k_c = \frac{t_s}{t_s - \gamma \delta_m} \quad (18)$$

in which

$$t_s = 2 \frac{\pi R_s}{N_s} \quad (19)$$

$$\gamma = \frac{4}{\pi} \left[\frac{s}{2\delta_m} \tan^{-1}\left(\frac{s}{2\delta_m}\right) - \log \sqrt{1 + \left(\frac{s}{2\delta_m}\right)^2} \right] \quad (20)$$

δ_m is the air gap between the rotor and the stator:

$$\delta_m = R_s - R_m \quad (21)$$

k_c is the Carter's coefficient, which accounts for the reduced flux through each tooth due to the slotting effect, and s denotes the gap between the teeth crowns.

From eqns. (7) and (15), it follows that the coupling factor between the mechanical and electrical equations is given by:

$$\hat{\theta} = - \sum_{n=1,3,5,\dots}^{\infty} \frac{1}{k_c} n p h N_f K_n T_n \cos(np\varphi) \quad (22)$$

The internal resistance and inductance of the coil can be determined from its shape. The former can be calculated by:

$$R_{int} = \frac{\rho l}{A_w} \quad (23)$$

where l is approximated by:

$$l = 2N_f(h + w) \quad (24)$$

A_w is the cross sectional area of the wire.

The inductance, L , is approximated using the formula by Joo et al [19] for the inductance of a single phase brushless DC motor:

$$L = \mu_0 R_s h \frac{4\pi N_f^2}{(2p)^3} \int_0^{\frac{2\pi}{2p}} \frac{1}{t_{gap}} d\varphi \quad (25)$$

Parametric Study

In the present study, the above equations of motion are solved to produce the frequency-response curve using AUTO bifurcation analysis software [20] with RAUTO [21]. Inspection of the equations of motion shows that there are seven variables that may affect the response of the energy harvester:

- Mass moment of inertia of the rotor, J
- Linear coefficient of stiffness, k_1
- Nonlinear (cubic) coefficient of stiffness, k_3
- Mechanical damping, c_{mech} .
- Electromechanical coupling factor, $\hat{\theta}$
- Electrical resistance, R_{int} and R_{Load}
- Coil inductance, L

The above variables depend on physical design parameters, such as the length of the energy harvester and radius, which will be discussed in the following sections.

Inertia

Moss et al [22] showed that power generation is linearly proportional to the harvester's moving mass in a study of 68 electromagnetic energy harvesters reported in literature. In the present application, the maximum inertia (and therefore the maximum power) of the energy harvester is dictated by the physical space where it will be used. Cost and weight reduction are incentives to minimise the inertia of the system.

Linear Coefficient of Stiffness

For the energy harvester to produce sufficient power, it must be operating in the vicinity of resonance conditions. Altering the linear component of the stiffness allows tuning of the energy harvester to resonate at low shaft speeds. The linear stiffness required at the desired shaft speed is given by:

$$k_1 = \omega_n^2 J \quad (26)$$

Fig. 8 shows the relationship between the linear stiffness coefficient and the power output assuming all other parameters remaining constant. A linear relationship with negative slope is noted between the linear stiffness and the cycle average power. Hence, the optimum value of k_1 is the minimum for which the jump-up frequency of the Duffing oscillator is greater than the minimum speed of the shaft.

Nonlinear Coefficient of Stiffness

The cubic component of the stiffness causes the system's response to behave like a duffing oscillator, as illustrated in Fig. 2 for various k_3 values. When the shaft speed is increased, the response follows the (upper) stable branch. If the excitation frequency exceeds the peak of the response (indicated on each curve), the response will jump-down to the lower energy branch. The dashed lines represent unstable solution branches that cannot be physically realized.

Fig. 2 shows that increasing the cubic nonlinearity stiffness coefficient has the effect of increasing the jump-down frequency of the nonlinear response. It is desirable from a design perspective that the driving frequency does not exceed the jump-down frequency, such that the solution always remains on the higher energy branch (higher energy may be harvested). Thus, using higher k_3 values would be preferable. However, the increase in cubic stiffness has the effect of reducing the amplitude of vibrations (hence, the power output) at a

given frequency. Therefore, an optimum k_3 value is the minimum value that still results in a higher jump-down frequency than the maximum operating frequency of the shaft.

With reference to Fig. 2, the curve corresponding to 1400 Nm/rad³ does not exhibit a jump-down frequency. Further simulations were run in which the excitation frequency was extended beyond reasonable limits and the expected jump-down frequency was never met. This effect can be appreciated by adapting the analytical model of Brennan et al [23] for calculating the jump-down frequency of a duffing oscillator as follows.

Due to the low frequencies (up to 133 Hz) experienced by the energy harvester and the low current (on the order of tens of milliamps) generated, the time rate of change of current is expected to be low. This, together with the low inductance (<10 mH) of the coil, suggests that it is reasonable to neglect the inductance term in eqn. (12) in order to use the approach demonstrated by Brennan et al [23]. Thus, eqn. (12) can be reduced to:

$$I = -\frac{\hat{\theta}\dot{\phi}}{R_{Load} + R_{int}} \quad (27)$$

Substituting eqns. (4) and (27) into eqn. (11) yields:

$$J\ddot{\phi} + k_1\phi + k_3\phi^3 + c_{mech}\dot{\phi} + \frac{\hat{\theta}^2}{R_{Load} + R_{int}}\dot{\phi} = 0.005\omega^2 J \cos(\omega t) \quad (28)$$

The above equation of motion can be written in non-dimensional form as:

$$y'' + 2\zeta y' + y + \varepsilon y^3 = \cos(\omega t) \quad (29)$$

where

$$y = \frac{\phi}{\phi_0}, \quad \varepsilon = \frac{k_3 \phi_0^2}{k_1}, \quad \zeta = \frac{c_{mech} + \frac{\hat{\theta}^2}{R_{Load} + R_{int}}}{2J\omega_n}, \quad \omega_n^2 = \frac{k_1}{J}, \quad \tau = \omega_n t, \quad \Omega = \frac{\omega}{\omega_n},$$

$$\phi_0 = \frac{0.005\omega^2 J}{k_1}$$

And $(\cdot)' = d/d\tau(\cdot)$. Brennan et al. [21] showed that the maximum displacement amplitude, Y_d , at the jump-down frequency can be approximated by:

$$Y_d \approx \left(\frac{2}{3\varepsilon} \left(\left(1 + \frac{3\varepsilon}{4\zeta^2} \right)^{\frac{1}{2}} - 1 \right) \right)^{\frac{1}{2}} \quad (30)$$

The jump-down frequency can be estimated as:

$$\Omega_d \approx \frac{1}{2^{\frac{1}{2}}} \left(1 + \left(1 + \frac{3\varepsilon}{4\zeta^2} \right)^{\frac{1}{2}} \right)^{\frac{1}{2}} \quad (31)$$

The following assumptions have been made: (i) Damping is small, such that $\zeta^2 \ll 1$ and (ii) Terms containing $\cos(3\Omega t)$ and higher can be neglected in the Harmonic Balance method. Substituting the expressions for ε and ϕ_0 into eqn. (31) yields:

$$\Omega_d \approx \frac{1}{2^{\frac{1}{2}}} \left(1 + \left(1 + \frac{7.5 \times 10^{-5} k_3 \omega^4 J^2}{4k_1^3 \zeta^2} \right)^{\frac{1}{2}} \right)^{\frac{1}{2}} \quad (32)$$

Eqn. (32) illustrates the dependence of the jump-down frequency on the excitation frequency. As the quantity

$\frac{7.5 \times 10^{-5} k_3 \omega^4 J^2}{4k_1^3 \zeta^2}$ becomes sufficiently large, such that $\frac{7.5 \times 10^{-5} k_3 \omega^4 J^2}{4k_1^3 \zeta^2} \gg 1$, the jump-down frequency becomes

approximately linearly proportional to the excitation frequency since k_1 , k_3 , J and ζ will be approximately constant for a given energy harvester at any speed.

When the excitation frequency exceeds the jump-down frequency, the solution will jump to the lower energy branch. This cross over point is illustrated in Fig. 3, where the curve corresponding to $k_3 = 1400 \text{ Nm/rad}^3$ represents a system without a jump-down frequency, whereas the curve corresponding to $k_3 = 700 \text{ Nm/rad}^3$ crosses the excitation frequency line, exhibiting a jump-down phenomenon at a shaft speed of 1566 rpm (corresponding to second order speed fluctuations at 52.2Hz).

The preceding analysis assumes that all terms other than the excitation frequency are constant. This is not the case for the electrical damping due to the dependence of the coupling factor on the relative displacement of the rotor. Thus, as the amplitude of vibrations increases, the total damping of the system will decrease.

However, the above analysis still gives an insight into the phenomenon that causes the drop-down frequency to be unreachable.

Fig. 7 (c) shows the relationship between the nonlinear stiffness coefficient and the power output of the energy harvester assuming all other parameters are held constant. The resulting relationship takes the form:

$$P_e = \frac{a}{k_3^{1/2}} + \frac{b}{k_3^{1/4}} + \frac{c}{k_3^{1/8}} \quad (33)$$

where a , b and c are constants determined by curve fitting. The power output decreases with increased cubic stiffness, hence the optimum is the lowest k_3 stiffness value for which an upper energy branch stable solution exists at the maximum shaft speed.

Mechanical Damping

The mechanical damping term arises due to friction in the bearings that support the rotor, friction in the springs and hysteresis and eddy current losses that may occur within the iron core of the stator. Previous works by Trimble et al [14] and Jang et al [24] have employed very similar electromechanical coupling methods as in the present work, namely a permanent magnet motor where the rotor oscillates around the stator due to a spring element. In Trimble et al [14], a Quality factor of 60 was experimentally determined which equates to damping ratio of 0.83%. Jang et al devised a variable stiffness energy harvester for translational vibrations in which a proof mass rotates a shaft connected to an electric motor. They measured a rotary damping coefficient of 6.604×10^{-3} Nms. Three system stiffness values (and corresponding inertias) were tested which result in damping ratios of 2.68%, 3.14% and 4.02%. These values are significantly higher than the damping ratio of Trimble et al [14]. Although the inertia of the rotor in Trimble et al [14] is not specified, the inertia stated in Jang et al [24] is in the range $1.268\text{E-}3 - 1.694\text{E-}3$ kg m² which is nearly two orders of magnitude higher than the expected inertia of the rotor in the present study. Also, the present study concerns frequencies in the range 23 -133 Hz compared to the frequencies around 1 Hz in the work of Jang et al [24]. The reduced inertia of the present work will increase the damping ratio for a constant damping coefficient whereas the increased resonant frequency is expected to reduce the damping ratio.

Furthermore, the works of Trimble et al [14] and Jang et al [24] both use steel spring elements whereas in the present work the spring element with a cubic stiffness is to be realised using elastomeric material which has higher internal losses due to hysteresis, thus leading to higher damping ratio. For example, in the work of Luo et al [25], a damping ratio of 9.19% was measured. Therefore, in the present work, a conservative estimate of the damping ratio is assumed to be 5% throughout. A more accurate value will need to be determined experimentally when a physical prototype is manufactured.

Electromechanical coupling factor, electrical resistance and coil inductance

To predict the optimisation of the coupling factor, it is once again assumed that the effects of the coil inductance are negligible such that eqn. (28) can be used to describe the motion of the rotor. The electromechanical coupling term can be considered as damping in the mechanical system and, therefore, the electrical damping can be approximated from the equation of motion:

$$c_{elec} = \frac{(\hat{\theta})^2}{R_{Load} + R_{int}} \quad (34)$$

It is found that both the coupling factor and internal resistance depend on the number of coil turns.

Substituting eqns. (22) and (23) into eqn. (34) returns:

$$c_{elec} = \frac{\left(-N_f \sum_{n=1,3,5,\dots}^{\infty} \frac{1}{k_c} nphK_n T_n \cos(np\varphi)\right)^2}{\frac{2\rho N_f (h+w)}{A_w}} \quad (35)$$

The load resistance has been assumed to be equal to the internal resistance of the coil. Simplification gives rise to the following equation which shows that the electrical damping is linearly dependent on the area of the conductor. All other terms are a function of the geometry and material properties:

$$c_{elec} = \frac{N_f A_w \left(\sum_{n=1,3,5,\dots}^{\infty} \frac{1}{k_c} nphK_n T_n \cos(np\varphi)\right)^2}{2\rho(h+w)} \quad (36)$$

The above is re-written as:

$$c_{elec} = \frac{N_f A_w \hat{\theta}_0^2}{R_{int_0}} \quad (37)$$

where the per-turn coupling factor, $\hat{\theta}_0$, and per turn resistance, R_{int_0} are given as:

$$\hat{\Theta}_0 = \left(\sum_{n=1,3,5,\dots}^{\infty} \frac{1}{k_c} nphK_n T_n \cos(np\varphi) \right) \quad (38)$$

$$R_{int_0} = 2\rho(h + w) \quad (39)$$

Eqn. (36) reveals that the geometry of the generator and the area of the conductor are significant for the calculation of power. If the inductance term remains negligible, it is beneficial to have as many turns as possible to increase the generated voltage which will aid rectification of the generated AC voltage. Furthermore, the per-turn coupling factor and internal resistance are only dependent on the geometry of the energy harvester and various material properties; hence, if lower damping is required, it can be easily attained by reducing the area of the conductor.

To obtain an optimum coupling factor and internal resistance for the examined harvester inertia, an optimisation of the energy harvester geometry must be conducted. For fixed inertia, the radius of the rotor can be varied and the corresponding rotor length is calculated. The coupling factor and internal resistance are then determined over a range of radii. For this process, several assumptions are necessary regarding the variables involved in the coupling factor in equation (22):

- R_{int} and R_{Load} : the internal resistance is dependent on the resistivity of the conductor and the geometry of the stator as in eqn. (39). The internal resistance is set equal to the load resistance for maximum power transfer to the load.
- t_{mag} , t_{gap} : as the magnet thickness is reduced, its length must be increased to maintain a constant inertia. Thus, due to the inertia being proportional to the square of the radius and linearly proportional to length, the optimum magnets should be long and thin. Consequently, it is assumed that the magnets are always 1 mm thick (for all inertia and radii values). Assuming all iron

reluctances are negligible, the magnetic energy supplied to the air gap is at maximum when the magnet energy product BH is at maximum as well [26]. Since the operating point of the magnet depends on the air gap (the magnet's magnetic load), there exists an optimum air gap for electromagnetic coupling, where the magnet operates at its optimum point.

- Fig. 4 shows the variation of the maximum electrical damping with respect to air gap.
- N_f, d_w : the usable area of the conductor in the coil windings is assumed to be 70% of the geometrically available area due to windage and the enamel coating on the copper. Collectively, the number of coil turns and the wire diameter represent a function of the total cross-sectional area of the conductor that electrical damping is linearly dependent on. The induced emf is linearly dependent on the number of coil turns, so ideally the thinnest possible wire and highest number of turns are desirable.
- B_r : the coupling factor is linearly dependent on the remnant magnetic flux density of the magnet material used. The remnant magnetic flux is assumed to be constant at 1.3 T for all conditions, which corresponds to the expected remnant magnetic flux of an N42 grade NeFeB magnet.
- e_c, w_t : the minimum achievable thickness of the stator core teeth crown, e_c , is assumed to be 1.3 mm due to manufacturing tolerances. The minimum stator tooth width, w_t , is assumed to be 2.6 mm to account for the flux from both sides of the crown. Both dimensions may need to be thicker to prevent saturation (calculated below). Thick teeth are undesirable because they reduce the area available for the conductor, hence reducing the electrical coupling.
- s : denotes the gap between the stator teeth. A smaller gap between teeth allows more flux to pass through the tooth which in turn slightly increases the coupling factor. Throughout this work, the slot opening is assumed to be at minimum 1 mm due to manufacturing tolerances.

- B_s : the saturation flux density of material, used to determine the minimum tooth dimensions to avoid saturation.
- h : the magnet length. Not all the rotor inertia is assumed to be used by the active volume (magnets). The rest is necessary for bearings, backing iron and the structure required to mount the rotor to the bearings. The minimum magnet length is assumed to be ten times larger than the air gap to ensure the long, uniform magnetic field distribution along its length in accordance with the 2D magnetic field modelling assumptions.

Markovic and Perriard [16] have presented a method for calculating the minimum thickness of the stator core and backing iron that can accept enough flux from the magnets, such that the assumptions of infinitely permeable iron and no saturation are valid for the previous analysis. A neat feature of the energy harvester compared to a regular motor is that the magnets do not necessarily line up with the stator teeth. As a result, the teeth can be thinner, since they do not need to accept as much flux as a normal motor. Each tooth must be wide enough to accept the magnetic flux through it when the magnet is in its most extreme position. During the simulation, the tooth width and crown thickness are calculated using the method of Markovic and Perriard [16]. With the dimensions of the stator and rotor known, the maximum area available for coils can be calculated. Then the maximum coil conductor area is multiplied by the ratio $\hat{\Theta}_0^2/R_{int_0}$ to obtain the maximum electrical damping constant.

Optimisation Results and Discussion

To validate the presented numerical model, the analytical methods of Brennan et al [23] are compared to the drop-down frequencies observed in Fig. 2. Table 1 shows the values of the parameters used in the simulations.

Table 2 shows the results of substituting these values into Eqn. (32) compared to the drop-down frequencies observed numerically. The analytical solution used damping ratio of $\zeta = 0.093$ to account for both the mechanical and electrical damping. The numerical and analytical solutions agree to within 2% for the 450 and 700 Nm/rad³ cases and the drop-down frequency for the 1400 Nm/rad³ case is infinite for both solutions, thus the numerical model was deemed accurate.

Due to the broad operating frequency range of the rotating shaft, it is necessary to evaluate the power generation over the whole assumed drive cycle to ensure that power can be constantly supplied to the wireless sensor node. Since the intended application is drivetrains, a suitable rotational speed cycle upon which this analysis was based is the Real Driving Emissions (RDE) test that involves real-world driving of an automobile for emissions testing [27]. Fig. 5 shows how the engine speed varies during the RDE test. This input data will be used to calculate the average power over a drive cycle. Arms et al [28] used power management techniques to reduce the power consumption of a wireless sensor node for strain gauge application from 45 mW at full speed (1700 samples/second wireless data transmission) to less than 900 μ W at 10 samples/second. In the intended application, sample rates as high as 1700 samples per second are desirable. Hence, it is assumed that the electrical power required from the energy harvester is 45 mW. Thus, it is important that the energy harvester averages at least 45 mW over the entire drive cycle. It is also expected that the storage device (battery or capacitor) is suitably sized to power the sensor during the times when power generation is less than 45 mW.

The first step in optimising the energy harvester is to assume an initial inertia value for the rotor assembly. Using this assumed inertia, the linear component of the torsional stiffness is estimated, giving rise to linear resonance at 700 rpm:

$$k_1 = \omega_n^2 J \quad (40)$$

In linear systems, it is known that the maximum power transferred to the load occurs when the electrical damping is equal to the mechanical damping of the system [29]. This is achieved when:

$$c_{mech} = c_{elec} \quad (41)$$

Therefore, the electrical damping of Eqn. (37) needs to be optimised to match the mechanical damping of the system. Fig. 6 (a) shows how the drop-down shaft speed, calculated using Eqn (31), varies with respect to cubic stiffness coefficient, k_3 , and the electrical damping ratio, ζ_e . The white area indicates harvester parameter combinations for which the drop-down frequency is infinite. All combinations corresponding to the grey shaded area represent harvesters with drop down frequencies below 2000 rpm, which is not acceptable for the examined application.

Eqn. (30) can be used to calculate the amplitude of vibrations at the drop-down frequency of the energy harvester. Assuming a solution of the form

$$\varphi = \Phi \sin(\omega t) \quad (42)$$

and differentiating with respect to time gives:

$$\dot{\varphi} = \omega \Phi \cos(\omega t) \quad (43)$$

The electrical power delivered to the load is given by:

$$P = \frac{V^2}{2R_{load}} \quad (44)$$

where the factor 2 appears because of the voltage divider effect between the matched internal resistance and load resistance. Substituting Eqn (7) into Eqn (44) yields:

$$P = \frac{(\hat{\Theta}\dot{\phi})^2}{2R_{load}} \quad (45)$$

For maximum power, the value of Φ calculated using Eqn. (30) is substituted into Eqn. (45), obtaining:

$$P_{max} = \frac{(\hat{\Theta}\omega\Phi)^2}{2R_{load}} \quad (46)$$

Plotting Eqn. (46) for k_3 and electrical damping ratio, ζ_e , gives rise to Fig. 6 (b) which shows a surface plot of power output. Fig. 6 (c) and (d) show the corresponding side views of Fig. 6 (b) from k_3 and ζ_e , respectively. The optimum cubic stiffness is found to be 1500 Nm/rad³, which agrees well with the value found in the preceding numerical analysis. The damping ratio ζ_e at the optimum power is 0.049, which is approximately the same as the mechanical damping of the system (the latter chosen to be 0.05). Better resolution in k_3 axis can provide a more accurate approximation of the optimum electrical damping ratio.

Cammarano et al [30] showed that an analytic equation for approximating the optimum damping ratio of a Duffing energy harvester is the same as that for a linear energy harvester. This finding agrees with those of Fig. 6, thus hereafter, the electrical damping is optimised by matching the mechanical damping.

Matching the electrical damping is achieved by altering the radius (and consequently the length) of the energy harvester together with the length of the air gap until the electrical damping is most closely matched to the mechanical damping. If the maximum electrical damping is too high, it can be reduced by reducing the area of the conductor. If the maximum electrical damping is insufficient, it can be increased by increasing the number

of coil turns whilst simultaneously reducing the diameter of the wire to ensure the total area of the conductor is unchanged.

Having chosen a trial inertia value with corresponding linear stiffness coefficient, mechanical and electrical damping, the nonlinear stiffness coefficient k_3 is now assumed and the corresponding frequency-response curve is calculated using AUTO bifurcation analysis software with RAUTO. The simulations provide the amplitudes of displacement, velocity and current vs excitation frequency. Once the jump-down frequency for the corresponding k_3 value is found, a new k_3 value is approximated based on previous iterations. The process repeats until k_3 converges toward the minimum value at which the jump-down frequency exceeds the maximum speed of the shaft.

Once the optimum value of k_3 is obtained for a given rotor inertia, the rms current is estimated by assuming sinusoidal current waveform:

$$I_{\text{rms}} = \frac{I_{\text{max}}}{\sqrt{2}} \quad (47)$$

The average power at each shaft speed is calculated by:

$$P_{\text{avg}} = I_{\text{rms}}^2 R_{\text{Load}} \quad (48)$$

The power at each stage of the drive cycle of Fig. 5 is estimated by interpolation of the power at each speed.

The power is then integrated over the drive cycle and is divided by the total cycle duration to get the cycle average power. The inertia can be modified and the process is repeated until the target power output is matched.

The above process (described in the flowchart of Appendix A) results in optimum inertia, coupling factor and stiffness to achieve the required output power.

Table 3 summarises the upper and lower limit values of the main variables used in the optimisation process.

The target is that the energy harvester operates between 700 and 4000 rpm, generating average power of 45 mW over the full drive cycle of Fig. 5. The resulting energy harvester properties are summarised in Table 4.

As also demonstrated in Moss et al [22], a linear relationship between inertia and power output can be observed in Fig. 7 (a). Since the target linear resonance frequency is the same for all conditions, the linear coefficient of stiffness is also linearly dependent on inertia. Thus, there is also a linear relationship between the optimum nonlinear coefficient of stiffness for the jump-down frequency and the inertia of the harvester, which can be appreciated by inspection of eqn. (32). The above observations are valid assuming that the electrical damping can be optimised to match the mechanical damping in the available design space.

Fig. 9 (a) shows the maximum relative displacement as a function of the engine speed of the optimised energy harvester. Fig. 9 (b) shows the maximum power generated variation with respect to the speed. The average power over the drive cycle of Fig. 5 is calculated using the power shown in Fig. 9 (b) at each shaft speed of the drive cycle. Integration of the power over time, divided by the maximum time of the drive cycle, yields the cycle average power which is 45 mW as targeted.

The bifurcation analysis using AUTO software calculates the stable solutions of the equations of motion at steady state. However, in real world applications it will not be possible to reach steady state conditions without first enduring some transients. To ascertain whether the energy harvester will be able to undergo these transients, the governing equations were numerically integrated using the Runge - Kutta method to obtain the time history response of the optimum energy harvester. Fig. 10 shows the time history of the

power generated over the drive cycle. Fig. 10 (c) shows the upper stable branch being sustained during an accelerating transient at around 519s whereas Fig. 10 (d) shows the upper stable branch being sustained during a decelerating transient.

Conclusions

In the current work, an electromagnetic torsional energy harvester for rotating shaft applications has been modelled numerically using 2D magnetic field analysis. The addition of a cubic nonlinear stiffness results in an energy harvester with Duffing oscillator frequency response and the effect of each of the variables involved in the design has been investigated. The frequency dependent excitation amplitude was shown to cause an infinite jump-down frequency if the cubic stiffness is sufficiently high.

A linear relationship between the inertia of the rotor and the power output has been observed, as predicted in the literature [22]. Furthermore, it has been observed that the optimum linear and cubic stiffness coefficients are linearly dependent on the rotor inertia. The geometry of the energy harvester must be optimised together with the number of coil turns such that the electrical damping matches the mechanical damping of the system.

A method for optimising the energy harvester has been outlined and an energy harvester for achieving average power of 45 mW over a typical shaft drive cycle has been designed. Moreover, the time integration of the governing equations showed that the upper branch of the frequency response should be maintained even through the transient parts of the drive cycle. The next steps include the design of the cubic nonlinear spring arrangement and manufacturing of a physical prototype to validate the foregoing analysis.

Nomenclature

A_w	Cross sectional area of the wire
B_r	Remnant magnetic flux of the magnets
B_{rad}	Radial component of the magnetic flux density
C_{elec}	Electrical damping coefficient
C_{mech}	Mechanical damping
e_c	Thickness of stator tooth crown
e_r	Thickness of rotor backing iron
h	Magnet length in axial direction
I	Electrical current
J	Mass moment of inertia of the rotor
k_1	Linear component of stiffness
k_3	Cubic component of stiffness
k_c	Carter's coefficient
K_n	Constant for calculation of the coupling factor
L	Inductance of coil
l	Length of copper wire used
M_n	Magnetisation vector
N_f	Number of turns per coil
N_s	Number of stator teeth
p	Number of poles

R_{int}	Internal resistance of coil
R_{Load}	Electrical load resistance
R_m	Magnet inner radius
R_r	Inner radius of magnet backing iron
R_s	Stator tooth outer radius
s	Gap between stator teeth crowns
t	Time
T_c	Electromagnetic coupling energy
t_{gap}	Air gap between stator and magnets
T_n	Constant for calculation of coupling factor
w	Width of stator tooth
α	Angular displacement of stator with respect to static global reference
β	Angular displacement of rotor with respect to static global reference
δ_m	Magnet thickness in radial direction
ε	Induced electro-magnetic flux
ζ	Damping ratio
$\hat{\theta}$	Electromagnetic coupling factor
μ_0	Permeability of the free space
μ_r	Relative permeability of the magnets
v	Pole arc to pole pitch ratio
ρ	Resistivity

φ	Relative displacement of rotor with respect to stator
Φ_m	Magnetic flux through stator coils
Ω	Mean speed of the stator
ω	Frequency of excitation
ω_n	Resonant frequency of the linear system

List of Abbreviations

emf	Electromotive force
frf	frequency response function

References

- [1] Hsu, J.-C., Tseng, C.-T., and Chen, Y.-S., 2014, "Analysis and Experiment of Self-Frequency-Tuning Piezoelectric Energy Harvesters for Rotational Motion," *Smart Mater. Struct.*, **23**(7), p. 075013.
- [2] Gu, L., and Livermore, C., 2010, "Passive Self-Tuning Energy Harvester for Extracting Energy from Rotational Motion," *Appl. Phys. Lett.*, **97**(8).
- [3] Khameneifar, F., Arzanpour, S., and Moallem, M., 2013, "A Piezoelectric Energy Harvester for Rotary Motion Applications: Design and Experiments," *IEEE/ASME Trans. Mechatronics*, **18**(5), pp. 1527–1534.
- [4] Zhang, Y., Zheng, R., Kaizuka, T., Su, D., Nakano, K., and Cartmell, M. P., 2015, "Broadband Vibration Energy Harvesting by Application of Stochastic Resonance from Rotational Environments," *Eur. Phys. J. Spec. Top.*, **224**(14–15), pp. 2687–2701.
- [5] Zhang, Y., Nakano, K., Zheng, R., and Cartmell, M. P., 2016, "Adjustable Nonlinear Mechanism System for Wideband Energy Harvesting in Rotational Circumstances," *J. Phys. Conf. Ser.*, **744**(1).
- [6] Gu, L., and Livermore, C., 2012, "Compact Passively Self-Tuning Energy Harvesting for Rotating Applications," *Smart Mater. Struct.*, **21**(1), p. 015002.
- [7] Roundy, S., and Tola, J., 2014, "Energy Harvester for Rotating Environments Using Offset Pendulum and Nonlinear Dynamics," *Smart Mater. Struct.*, **23**(10), p. 105004.
- [8] Yang, Y., Shen, Q., Jin, J., Wang, Y., Qian, W., and Yuan, D., 2014, "Rotational Piezoelectric Wind Energy Harvesting Using Impact-Induced Resonance," *Appl. Phys. Lett.*, **105**(5), pp. 2012–2016.
- [9] Zhang, J., Fang, Z., Shu, C., Zhang, J., Zhang, Q., and Li, C., 2017, "A Rotational Piezoelectric Energy

- Harvester for Efficient Wind Energy Harvesting,” *Sensors Actuators, A Phys.*, **262**, pp. 123–129.
- [10] Joyce, B. S., Farmer, J., and Inman, D. J., 2014, “Electromagnetic Energy Harvester for Monitoring Wind Turbine Blades,” *Wind Energy*, **17**, pp. 657–669.
- [11] Pillatsch, P., Yeatman, E. M., and Holmes, A. S., 2012, “Piezoelectric Rotational Energy Harvester for Body Sensors Using an Oscillating Mass,” *Proc. - BSN 2012 9th Int. Work. Wearable Implant. Body Sens. Networks*, pp. 6–10.
- [12] Pillatsch, P., Yeatman, E. M., and Holmes, A. S., 2014, “A Piezoelectric Frequency Up-Converting Energy Harvester with Rotating Proof Mass for Human Body Applications,” *Sensors Actuators, A Phys.*, **206**, pp. 178–185.
- [13] Mei, J., and Li, L., 2013, “Split-Electrode Piezoelectric Scavengers for Harvesting Energy from Torsional Motions,” *J. Phys. Conf. Ser.*, **476**, p. 012136.
- [14] Trimble, A. Z., Lang, J. H., Pabon, J., and Slocum, A., 2010, “A Device for Harvesting Energy From Rotational Vibrations,” *J. Mech. Des.*, **132**(9), p. 091001.
- [15] Kim, G. W., 2015, “Piezoelectric Energy Harvesting from Torsional Vibration in Internal Combustion Engines,” *Int. J. Automot. Technol.*, **16**(4), pp. 645–651.
- [16] Markovic, M., and Perriard, Y., 2007, “An Analytical Formula for the Back Emf of a Slotted BLDC Motor,” *Proc. IEEE Int. Electr. Mach. Drives Conf. IEMDC 2007*, **2**, pp. 1534–1539.
- [17] Owens, B. A. M., and Mann, B. P., 2012, “Linear and Nonlinear Electromagnetic Coupling Models in Vibration-Based Energy Harvesting,” *J. Sound Vib.*, **331**(4), pp. 922–937.
- [18] Zhu, Z. Q., and Howe, D., 1993, “Instantaneous Magnetic Field Distribution in Permanent Magnet

- Brushless DC Motors. IV. Magnetic Field on Load," IEEE Trans. Magn., **29**(1), pp. 152–158.
- [19] Dae-Suk, J., Kyungil, W., and Dae Kyong, K., 2012, "Calculation of Winding Inductances for a Single-Phase Brushless DC Machine," J. Magn., **17**(3), pp. 196–199.
- [20] Doedel, E., and Oldeman, B., 2009, "Auto 07p: Continuation and Bifurcation Software for Ordinary Differential Equations. Technical Report," Methods Mol. Biol., **930**(January), pp. 475–98.
- [21] Schilder, F., 2007, "RAUTO : Running AUTO More Efficiently," (April).
- [22] Moss, S. D., Payne, O. R., Hart, G. A., and Ung, C., 2015, "Scaling and Power Density Metrics of Electromagnetic Vibration Energy Harvesting Devices," Smart Mater. Struct., **24**(2), p. 23001.
- [23] Brennan, M. J., Kovacic, I., Carrella, A., and Waters, T. P., 2008, "On the Jump-up and Jump-down Frequencies of the Duffing Oscillator," J. Sound Vib., **318**(4–5), pp. 1250–1261.
- [24] Jang, S.-J., Kim, I.-H., Park, K., and Jung, H.-J., 2016, "An Enhanced Tunable Rotational Energy Harvester with Variable Stiffness System for Low-Frequency Vibration," Proc. Inst. Mech. Eng. Part C J. Mech. Eng. Sci., **230**(5), pp. 732–736.
- [25] Luo, J., Wierschem, N. E., Fahnestock, L. A., Jr, B. F. S., Quinn, D. D., Mcfarland, D. M., Vakakis, A. F., and Bergman, L. A., 2014, "Design , Simulation , and Large-Scale Testing of an Innovative Vibration Mitigation Device Employing Essentially Nonlinear Elastomeric Springs," (April), pp. 1829–1851.
- [26] Furlani, E. P., 2001, *Permanent Magnet and Electromechanical Devices : Materials, Analysis, and Applications*, Academic Press, San Diego, California.
- [27] "What Is the Real Driving Emissions (RDE) Test?" [Online]. Available: <http://www.caremissionstestingfacts.eu/rde-real-driving-emissions-test/#>. [Accessed: 10-Jul-2018].

- [28] Arms, S. W., Townsend, C. P., Churchill, D. L., Galbreath, J. H., Mundell, S. W., and Lane, H., 2005, "Power Management for Energy Harvesting Wireless Sensors," *Proc. SPIE Smart Struct. Mater.*, **5763**(March), pp. 1–9.
- [29] Mitcheson, P. D., Toh, T. T., Wong, K. H., Burrow, S. G., and Holmes, A. S., 2011, "Tuning the Resonant Frequency and Damping of an Electromagnetic Energy Harvester Using Power Electronics," **58**(12), pp. 792–796.
- [30] Cammarano, A., Neild, S. A., Burrow, S. G., Wagg, D. J., and Inman, D. J., 2014, "Optimum Resistive Loads for Vibration-Based Electromagnetic Energy Harvesters with a Stiffening Nonlinearity," *J. Intell. Mater. Syst. Struct.*, **25**(14), pp. 1757–1770.

Appendix A

The flowchart of the optimisation process to select the properties of the energy harvester is provided below:

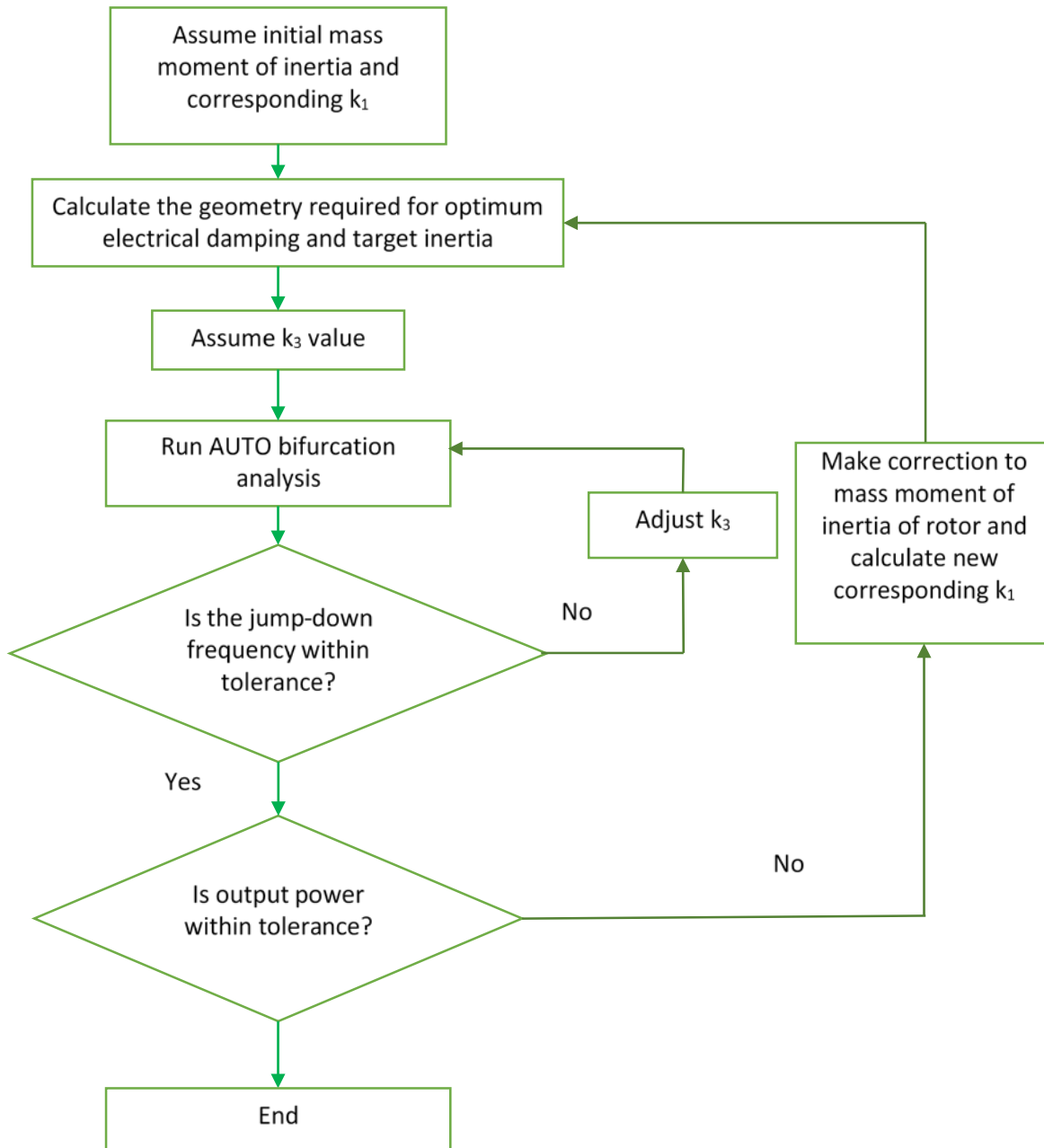


Figure Captions List

- Fig. 1 Schematic of the proposed energy harvester – N/S denotes the polarity of the magnet facing the stator core in a radial direction
- Fig. 2 Effect of the cubic nonlinearity on the vibration response of the harvester. The dashed lines represent unstable solution branches that cannot be physically realized.
- Fig. 3 Illustration of the jump-down frequency calculated using Eqn (32) for (i) $k_3 = 2000 \text{ Nm/rad}^3$ - no jump-down frequency and (ii) $k_3 = 960 \text{ Nm/rad}^3$ - jump-down frequency around 800 rpm
- Fig. 4 Variation of the electromagnetic damping with respect to air gap
- Fig. 5 The considered RDE drive cycle of the shaft
- Fig. 6 a) Effect of cubic stiffness and electrical damping ratio on drop down frequency, b) Effect of cubic stiffness and electrical damping ratio on power output c) Effect of cubic stiffness power output, d) Effect of electrical damping ratio on power output
- Fig. 7 Variation of the power output with respect to a) mass moment of inertia of rotor and c) cubic component of stiffness. b) shows the relationship between the optimum k_3 and the mass moment of inertia.
- Fig. 8 effect of k_1 on cycle average power with all other parameters constant
- Fig. 9 Frequency response curve of the optimized energy harvester - a) maximum angular displacement of the rotor and b) average power output
- Fig. 10 Time history of the optimized energy harvester throughout the drive cycle a) engine speed b) power output of harvester, c) time history of transient decreasing speed, d) time history of increasing shaft speed

Table Caption List

Table 1	Parameters used for calculation of solutions in Fig.2
Table 2	Comparison of AUTO model and analytical model
Table 3	Summary of the upper and lower limit values of the main variables used in the optimization process
Table 4	Optimized energy harvester properties

Figure 1

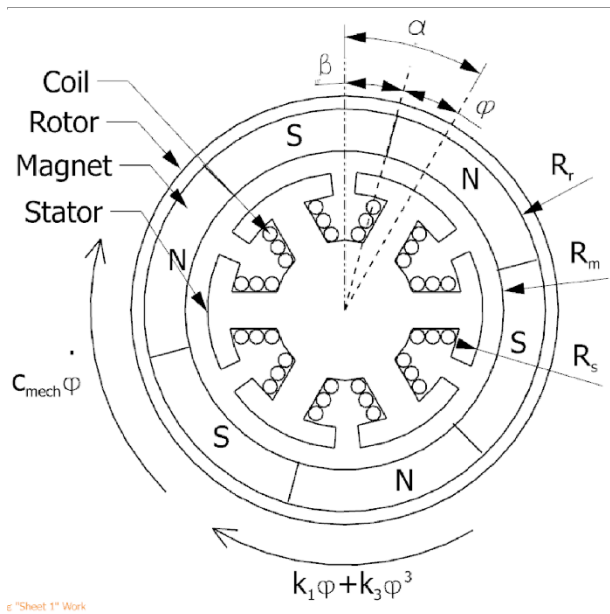


Figure 2

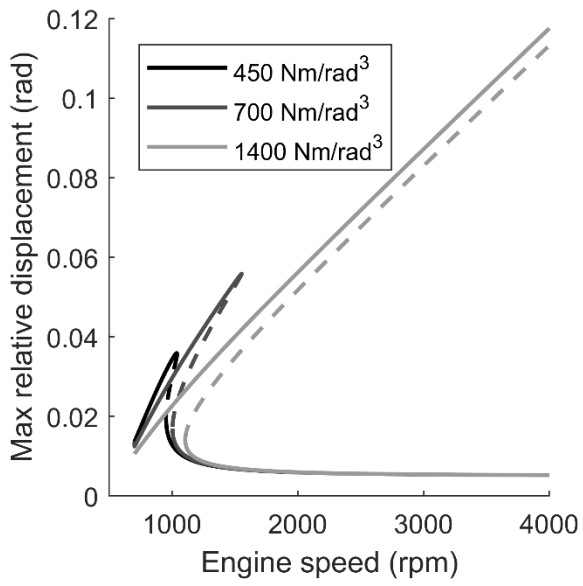


Figure 3

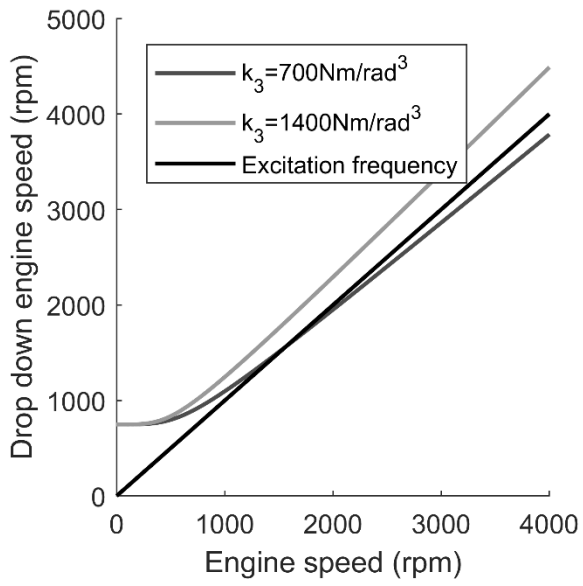


Figure 4

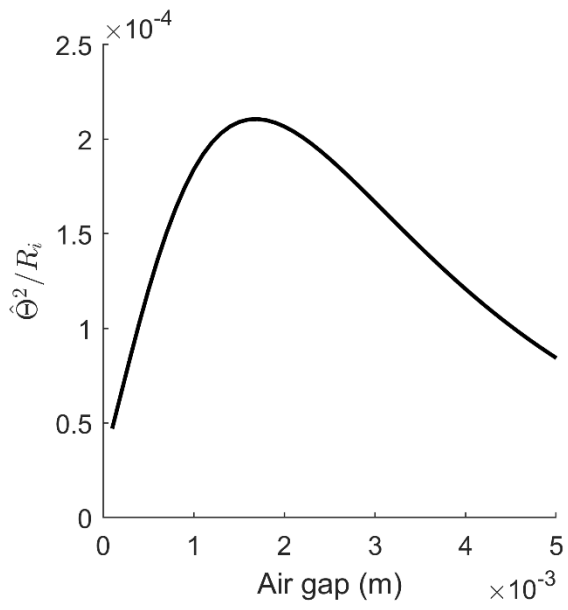


Figure 5

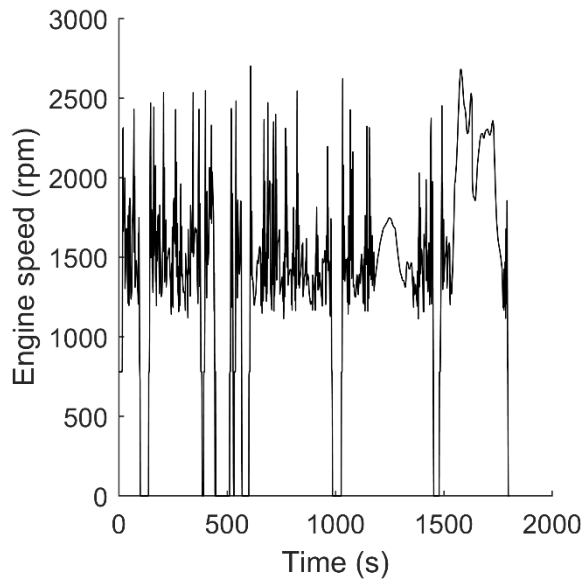


Figure 6

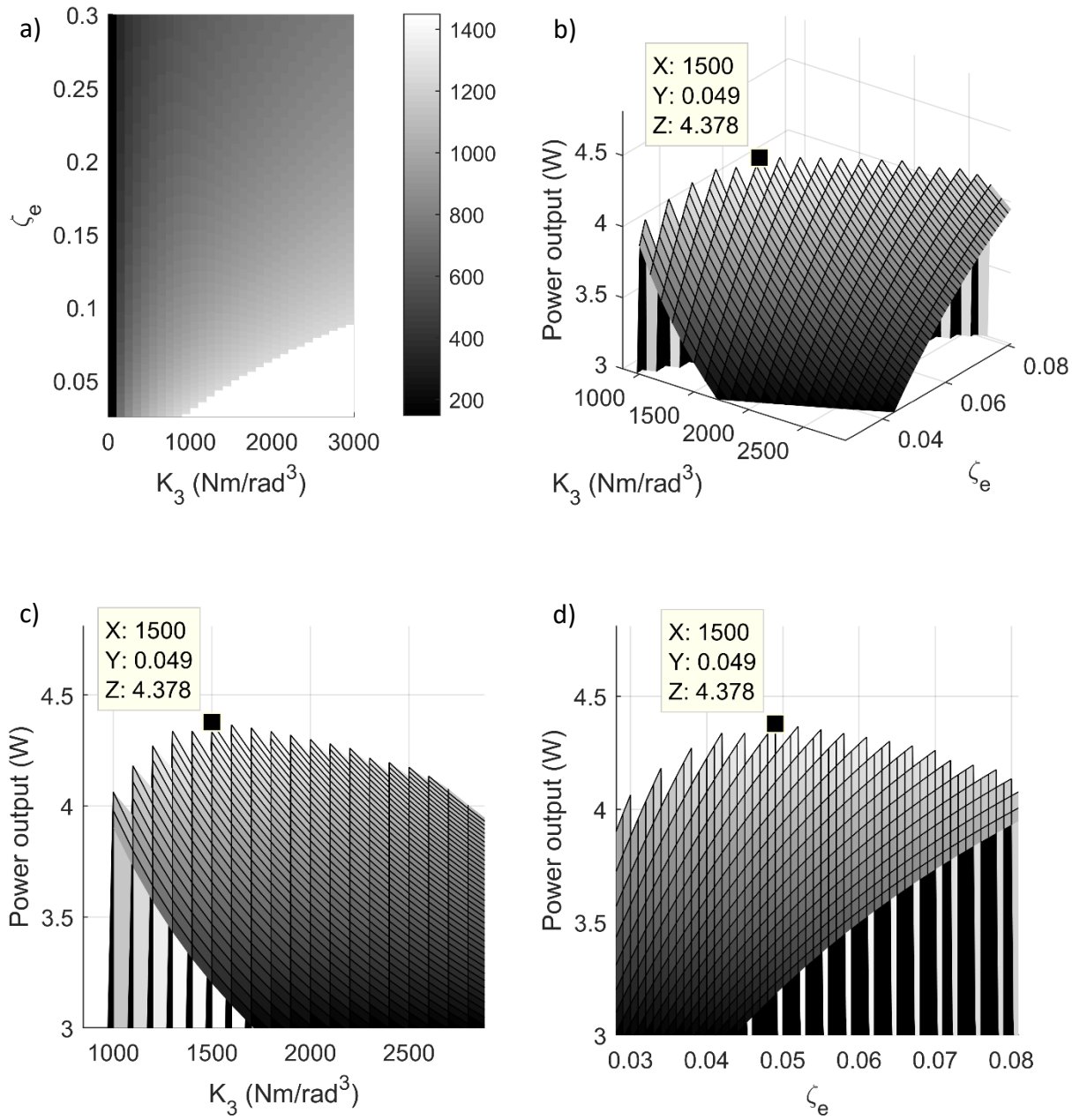


Figure 7

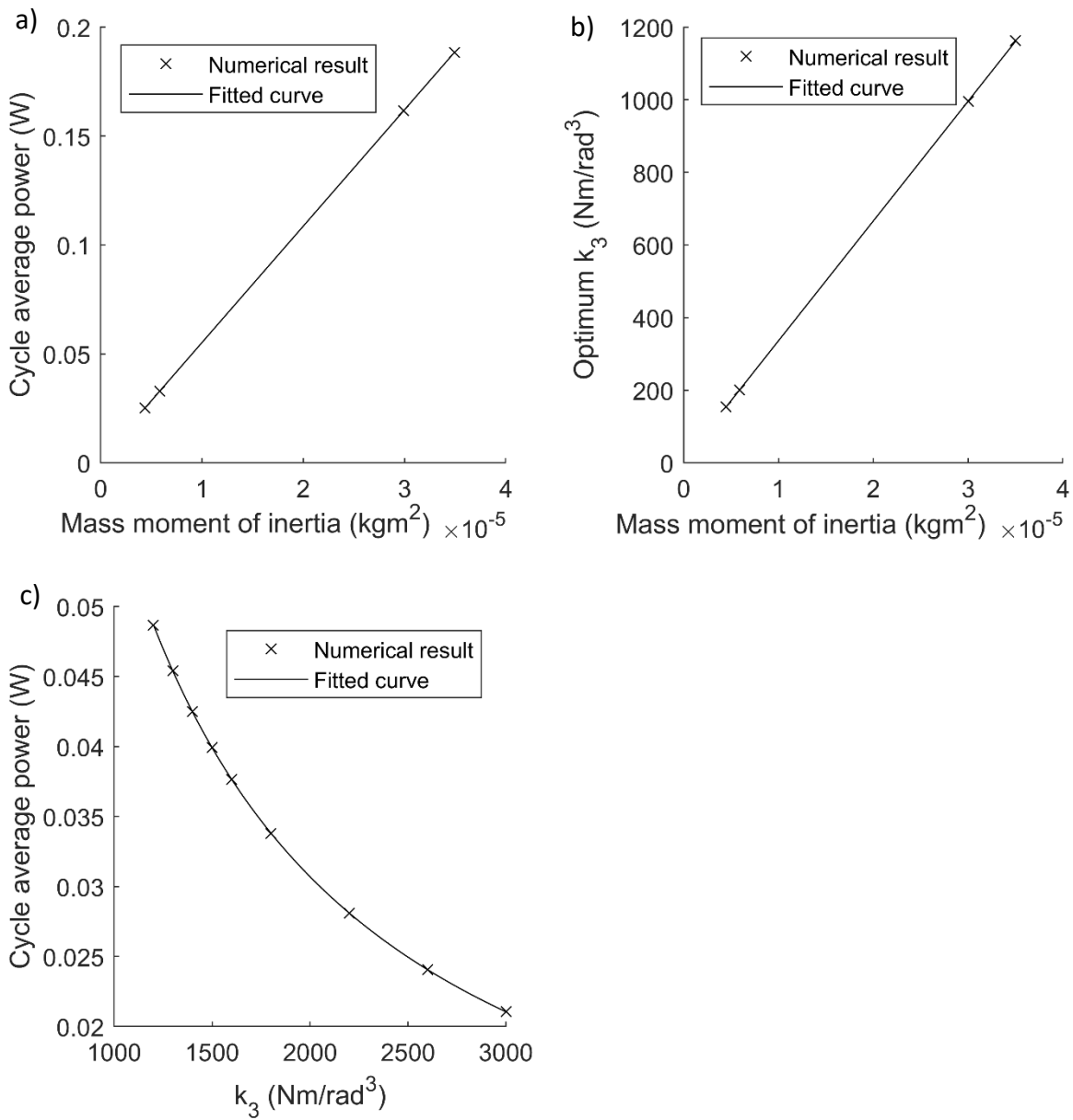


figure 8

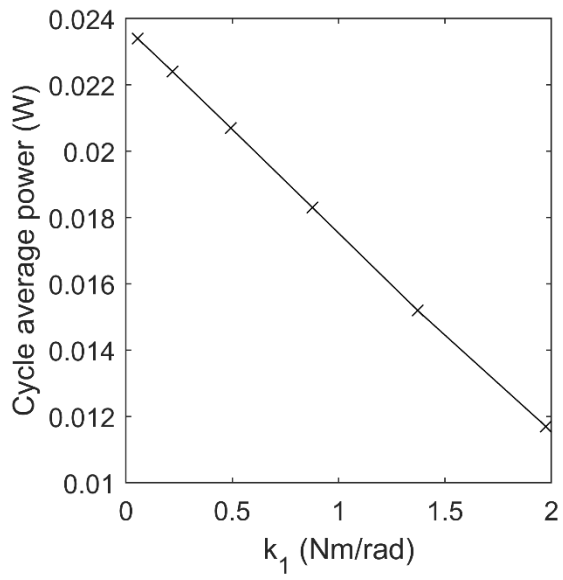


Figure 9

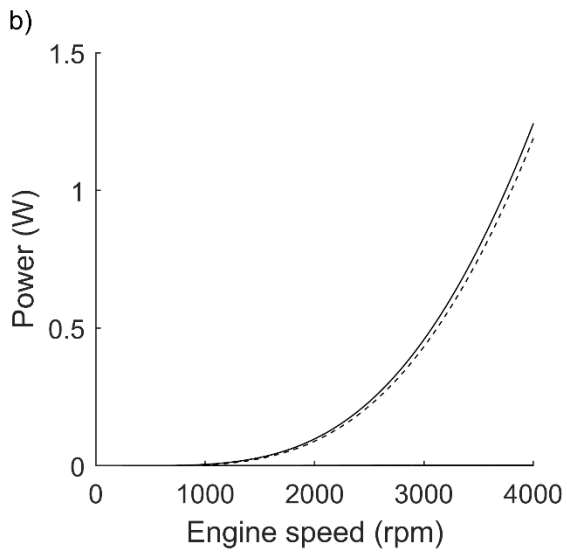
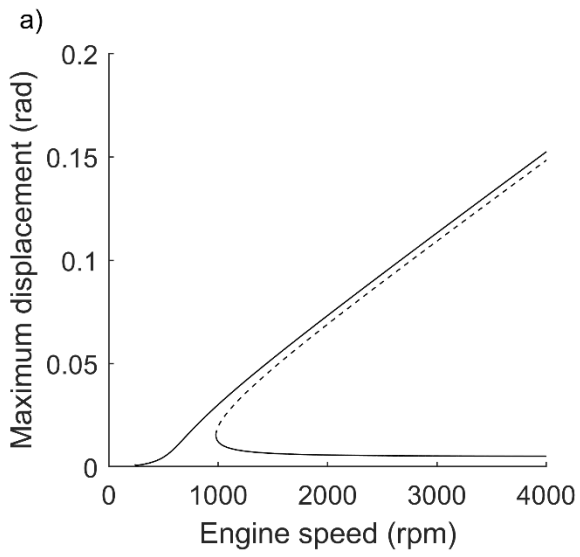


Figure 10

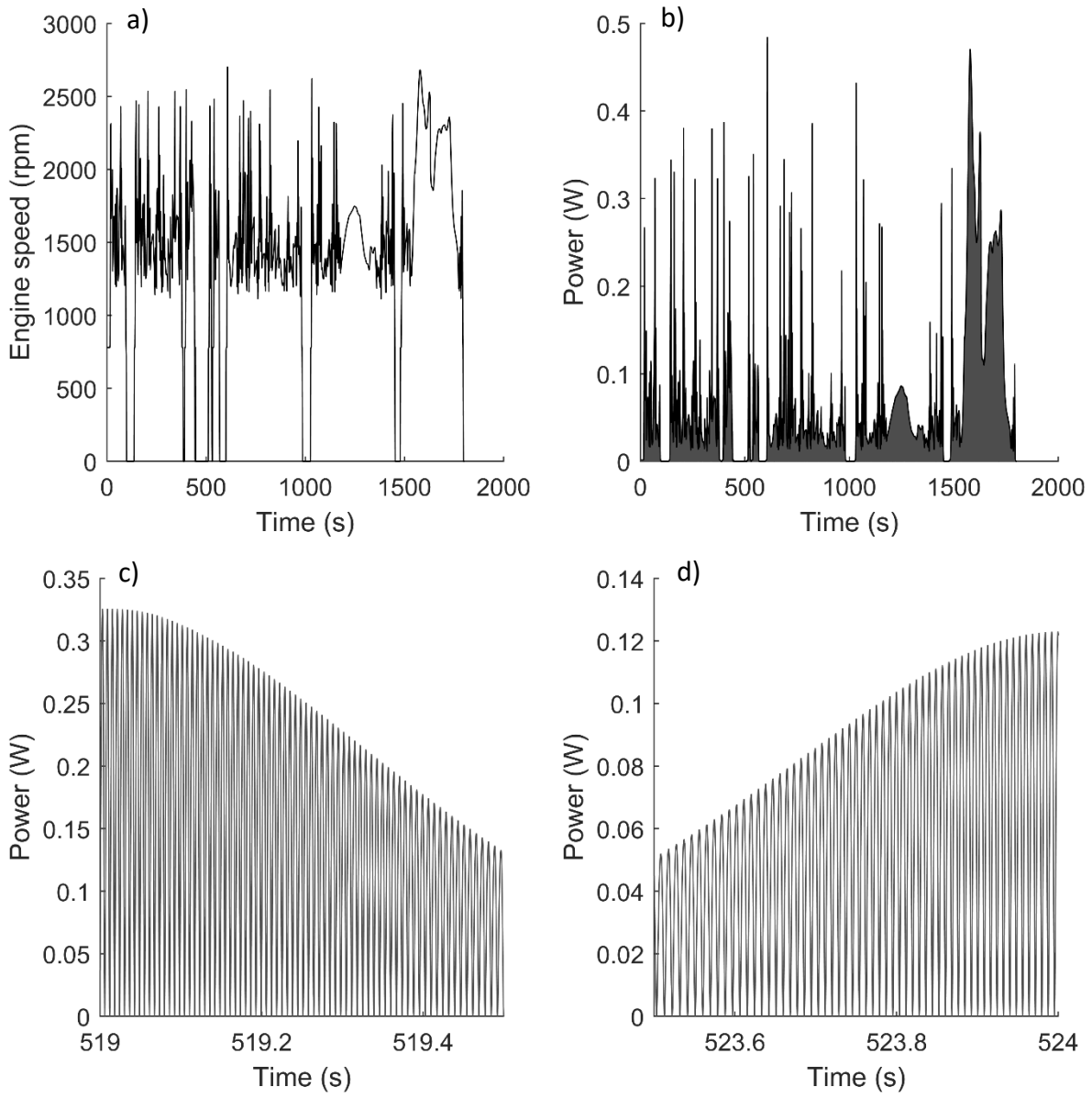


Table 1

Parameter	Value
Mass moment of inertia, J (kgm ²)	2E-5
Linear stiffness, k ₁ (Nm/rad)	0.492
Damping ratio, ζ	0.05
Coupling factor, $\widehat{\Theta}$ (Vs/rad)	0.2
Electrical resistance (Ω)	82.26
Electrical inductance (H)	0.16

Table 2

k ₃ (Nm/rad ³)	Drop-Down Shaft Speed (rpm)		Difference (%)
	Numerical model	Analytical model	
450	1056	1039	1.64
700	1566	1554	0.77
1400	∞	∞	-

Table 3

Parameter	Value
Minimum Stator radius (mm)	5
Maximum Stator radius (mm)	12
Minimum magnet length	$10 \times t_{mag}$
Maximum magnet length (mm)	50
Number of poles	6
Remnant magnetic flux density (T)	1.3
Saturation flux density (T)	1.7
Magnet arch to pole pitch ratio	1
Magnet thickness (mm)	1
Wire fill factor	0.7
Slot opening (mm)	1
Wire diameter (mm)	0.2
Damping ratio	0.05
Rotor inertia/active rotor inertia	2.5
Target average power per drive cycle (mW)	45
Target minimum jump-down shaft speed (rpm)	4000
Target resonant shaft speed of linear system (rpm)	700

Table 4

Parameter	Value
Average power output per drive cycle (mW)	44.00
Mass moment of inertia of rotor (kgm^2)	3.37E-5
Linear component of stiffness (Nm/rad)	0.7243
Cubic component of stiffness (Nm/rad ³)	1409.7
Inductance (mH)	160
Internal resistance (Ohm)	82
Stator radius (mm)	12
Air gap (mm)	1.00
Magnet length (mm)	27.27